

Numerical Simulation of Fracture Initiation in Barre Granite using an Experimentally Validated XFEM Model

Garg, Prasoon

Colorado School of Mines, Golden, Colorado, USA

Hedayat, Ahmadreza

Colorado School of Mines, Golden, Colorado, USA

Griffiths, D.V.

Colorado School of Mines, Golden, Colorado, USA

Copyright 2020 ARMA, American Rock Mechanics Association

This paper was prepared for presentation at the 54th US Rock Mechanics/Geomechanics Symposium held in Golden, Colorado, USA, 28 June-1 July 2020. This paper was selected for presentation at the symposium by an ARMA Technical Program Committee based on a technical and critical review of the paper by a minimum of two technical reviewers. The material, as presented, does not necessarily reflect any position of ARMA, its officers, or members. Electronic reproduction, distribution, or storage of any part of this paper for commercial purposes without the written consent of ARMA is prohibited. Permission to reproduce in print is restricted to an abstract of not more than 200 words; illustrations may not be copied. The abstract must contain conspicuous acknowledgement of where and by whom the paper was presented.

ABSTRACT: Fracturing in brittle rocks with an existing crack results in the development of a significant nonlinear region surrounding the crack tip called the fracture process zone. Various experimental and numerical studies have shown that the crack tip parameters such as the crack tip opening displacement (CTOD) and the fracture energy are critically important in characterizing the fracture process zone. In this study, numerical simulations of rock specimens with a center notch subjected to three-point bending were conducted using the extended finite element method (XFEM) along with the cohesive zone model (CZM) to account for fracture process zone. The input parameters of CZM such as the elastic and critical crack opening displacements were first estimated based on the results of three-point bending tests on the center notched Barre granite specimens. Displacements were measured using the two dimensional digital image correlation technique and used to characterize the evolution of the fracture process zone and estimate the parameters of the cohesive zone model. The results from the numerical simulations showed that CZM provided a good agreement with experimental data as it predicted all three stages of cracking from fracture process initiation to macro-crack growth.

1. INTRODUCTION

Quasi-brittle materials such as rock and concrete exhibit a significant nonlinear region surrounding the crack tip (Labuz et al., 1987). The non-linear zone is attributed to the concentrated micro-cracking zone (Labuz et al., 1987; Bazant and Planas, 1998), also known as the fracture process zone (FPZ). In laboratory experiments, the evolution of FPZ is critical as the assumption of small-scale yielding (i.e., small FPZ relative to crack length) is often violated (Bazant and Planas, 1998; Tarokh et al., 2017).

Several crack initiation and propagation criteria have been developed based on the stress-, strain-, and energy fields at the tip of the flaw (Goncalves and Einstein, 2013). However, most of these criteria are based on linear elastic fracture mechanics (LEFM) and, therefore, do not account for the fracture process zone (Xie et al., 2017). In recent years, the cohesive crack model has been widely used to characterize the fracture process zone in rocks (Ha et al., 2015; Lin et al., 2019a-b; Zhang et al., 2019). The cohesive crack model that was originally proposed by Hillerborg et al. (1976), considered an equivalent crack composed of a traction-free part and a process zone and was used to obtain a better estimate of the fracture energy of the material (Hillerborg et al., 1976; Lin et al., 2019b; Zhang et al., 2019).

The FPZ typically composed of micro-crack can be observed as white patches in some rocks such as Carrara marble and Barre granite (Wong and Einstein 2009a; Morgan et al., 2013). However, it is difficult to detect the FPZ through visual detection techniques such as optical microscopic imaging, as it is known to show cracking at the microscopic scale at different stress level (Lu et al., 2019; Li and Einstein, 2017). Alternatively, experimental techniques such as computer tomography (Ghamgosar and Erarslan, 2019), speckle interferometry (Lin et al., 2009), and digital image correlation (DIC) (Lin et al., 2014) have been successfully used to study the FPZ. Various studies (Ji et al., 2016; Zhang et al., 2018; Lin et al., 2019a-b) using DIC have characterized the evolution of FPZ in three stages namely; (1) elastic phase, (2) formation and propagation of FPZ, and (3) macro-crack initiation. However, there is no consistent method to pinpoint the transition between three stages. For instance, most studies (Lin and Labuz, 2013; Zhang et al., 2018; Lu et al., 2019) assumed that traction-free crack (macro-crack) initiates at the peak load that leads to decrease in global load. However, other studies such as Aggelis et al. (2013), Yu et al. (2018), Lin et al. (2019b) based on the combination of AE and DIC techniques have found that the FPZ is partially developed at the peak load. Thus traction free crack initiation occurs during the post-peak stage of the test.

Several numerical techniques such as the displacement discontinuity method (DDM) (Bobet and Einstein, 1998; Goncalves and Einstein, 2013), the numerical manifold method (NMM) (Wu and Wong, 2013), the discrete element method (DEM) (Zhang and Wong, 2012) and the extended finite element method (XFEM) (Sharafisafa and Nazem, 2014) have recently been utilized to simulate the crack initiation and propagation in various rock types. Specifically, XFEM based on the partition of unity (PU) method (Moes and Belytschko, 2002) has attracted considerable attention due to its effectiveness in modeling discontinuities in various problems such as interface growth and crack propagation (Belytschko and Black, 1999; Ha et al., 2015). In the conventional FEM, modeling discontinuities such as cracks requires conformity of the mesh to the geometric discontinuities (Khoei, 2014). The XFEM alleviates these problems by using the concept of partition of unity method, which allows elements that are intersected by discontinuities to be locally enriched while retaining properties of the stiffness matrix of the standard FEM (Moes and Belytschko, 1999).

In recent years, the XFEM has been widely used for modeling of rocks and specifically the crack growth under both tensile loading and compressive loading with decent success (Sharafisafa and Nazem, 2014; Eftekhari et al., 2017; Xie et al., 2017). For instance, Sharafisafa and Nazem (2014) simulated the crack growth in the Carrara marble under uniaxial compression using XFEM.

In this study, a consistent method based on the evolution of crack tip opening displacement (CTOD) estimated from DIC analysis was developed to characterize the FPZ and estimate the cohesive zone model parameters for Barre granite. A series of three-point bending tests were conducted on center-notched specimens. Further, the cohesive zone model was validated using XFEM based simulation of three-point bending tests in ABAQUS.

2. DIGITAL IMAGE CORRELATION (DIC)

DIC is one of the most frequently-used non-contact optical methods to measure in-plane deformation and strains of a planar surface (Hedayat et al. 2014a-c; Shirole et al., 2020b). In DIC, unique speckles are tracked between two digital images of a specimen surface (Sutton et al. 2009; Pan et al. 2009b) in the undeformed (or reference) and deformed states.

For DIC analysis, the stochastic pattern of gray-scale For DIC analysis, a stochastic pattern of gray-scale intensity values is first applied on specimen surface using a variety of techniques such as spray painting (Hedayat et al., 2014a) to ensure accurate image correlation. First, a region of interest (ROI) is defined in the reference image, which is further divided into evenly spaced grid points.

The motion of each grid point is assessed by tracking the subset around it between the original and deformed images. The subset is chosen rather than a single point because it contains a broader variation of gray-scale intensity values that can be uniquely identified in the deformed images (Sutton et al., 2009; Hedayat et al., 2014a). For image correlation, it is assumed that gray-scale intensity values in the subsets are preserved during specimen deformation. Thus each subset can be located in a deformed image with a certain degree of similarity (Shirole et al., 2020b). A statistical correlation criterion is used to evaluate the degree of similarity between the reference and deformed subsets. The position of the deformed subset with respect to the reference subset is located by identifying the peak position in the distribution of the correlation coefficient (Hedayat et al., 2014b; Shirole et al., 2019a). The displacement computed from the correlation procedure is then assigned to the center of the subset. The full-field displacement is obtained by following the same procedure for each grid point in the ROI (Pan et al. 2009).

In this study, 2D-DIC was used to characterize the fracture process zone (FPZ) by analyzing the evolution of full-field displacements. Further, cohesive zone model parameters such as the crack opening displacements were estimated using DIC to quantify the evolution of FPZ.

3 XFEM

Since its inception by Belytschko and Black (1999), the XFEM has been widely used in various fracture mechanics problems due to its ability to account for a discontinuous displacement field around the cracks. In conventional FEM, cracks can only propagate along element edges and thus required remeshing with the formation of new cracks (Moes and Belytschko, 2002). In the XFEM, a standard FE mesh for the problem is first created without accounting for any geometrical discontinuities. The presence of cracks or voids is then represented independently of the mesh by adding enrichment functions and additional degrees of freedom to the elements intersected by the crack (Karihaloo and Xiao, 2003; Moes and Belytschko, 2002; Sharafisafa and Nazem, 2014). The discontinuity is then included in the numerical model without a need for modifying the mesh. In the XFEM, displacement of the point x located in the domain containing a crack is approximated as follows (Belytschko and Black, 1999; Khoei, 2014):

$$u^h(x) = \sum_{i=1}^n N_i(x) u_i + \sum_{j=1}^m N_j(x) \psi(x) a_j \quad (1)$$

where both $N_i(x)$ and $N_j(x)$ are the standard FEM shape functions, u_i is the nodal displacement, a_j is the added set of degrees of freedom to the standard FEM, $\psi(x)$ is the enrichment function, n is the set of all nodal points of the domain, and m is the set of nodes of the elements located on the discontinuous boundary. The global enrichment function $\psi(x)$ has two components, namely the Heaviside function and the tip enrichment (Figure 1), to account for the displacement jump across crack faces and asymptotic singular fields near the crack tip (Xie et al., 2017). The displacement field in Eq. (1) can be rewritten as:

$$u^h(x) = \sum_{i=1}^n N_i(x) u_i + \sum_{j=1}^{m^1} N_j(x) H(x) a_j + \sum_{k=1}^{m^2} \left[N_k(x) \sum_{l=1}^4 F_l(x) b_k^l \right] \quad (2)$$

where m^1 and m^2 are the nodal subsets representing crack faces and the crack tip, respectively (Figure 1). The $H(x)$ is the Heaviside function for modeling a displacement jump across crack faces and $F_l(x)$ are the crack-tip functions; a_j and b_k^l are the degrees of freedom of the node enriched with displacement jump and the crack-tip functions, respectively. The tip enrichment and jump function appear in the element stiffness matrix.

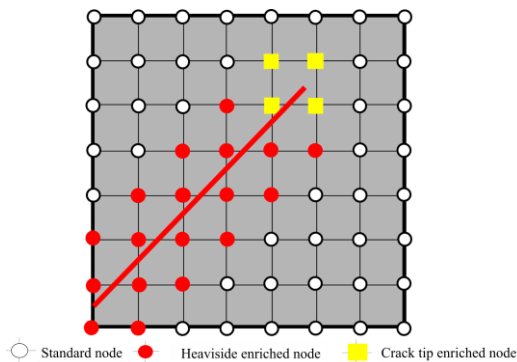


Figure 1. Enriched elements in the XFEM (after Xie et al., 2017).

4. EXPERIMENTAL DESIGN

4.1 Specimen Preparation

A series of three-point bending tests were conducted on Barre granite beams with the center notch for mode I loading (figure 2a). The Barre granite is a crystalline rock typically formed in the Devonian New Hampshire pluton series located in Burlington, Vermont (USA) (Iqbal and Mohanty, 2007; Nasser et al., 2010). It is primarily composed of feldspar (65%) and quartz (25%), with the average grain size of 0.87 mm (Shirole et al., 2020b). Due to its crystalline nature, the Barre granite rock has a negligible porosity of 0.6% and a density of 2.59 g/cm³ (Iqbal and Mohanty, 2007). Prismatic specimens

measuring 150 mm long, 75 mm wide, and 25 mm thick were prepared from a large block of Barre granite by sawing. All the surfaces of the specimen were then ground to ensure the desired dimension with tolerance to +0.20 mm and smoothness with the tolerance of Δ/d of 0.0043 mm in accordance with the ASTM D4543. The center notch of 25.8 mm in length and 1.02 mm in aperture was created by the Colorado WaterJet Company for each specimen.

4.2 Experimental Setup and Testing

The three-point bending tests were performed on the center-notched Barre granite specimens using an MTS servo-controlled loading machine. The specimens were loaded at the constant axial displacement rate of 0.2 $\mu\text{m}/\text{sec}$ to ensure stable crack propagation in the post-peak region. Additionally, the crack mouth opening displacement (CMOD) was measured by an extensometer called clip gauge bonded to the bottom surface of the beam. The extensometer measured the displacement between two clips across the gauge length of 12 mm.

During each test, digital images of the speckled surface of the specimen were captured at the rate of 12 frames/sec. The images were recorded by a CCD (Charged-coupled device) camera with 2448 by 2048 square pixels in combination with a Fujinon lens of 17.5 mm focal length (Model CF35HA-1). The Pylon Viewer software was used to control the camera and acquire the images. The images were then analyzed using the Correlated Solutions software in order to obtain the full-field surface displacements on the ROI, which was set as the small area of 40 \times 70 mm² around the center notch, as shown in figure 2b. The software required two inputs of the subset size and the step size. The subset size of 30 pixels was selected based on the recommendation of Sutton et al. (2007). Step size defines how far apart the tracking points are placed in the specimen. A smaller step size results in higher subset overlapping and provides the large oversampling required for accurate and detailed measurements of the displacement field (Hedayat et al., 2014b; Shirole et al., 2019a-b). The step size of 5 pixels was selected for optimal computational efficiency and high strain resolution (Shirole et al., 2020b). Additionally, an isotropic magnification factor (M) of 50 $\mu\text{m}/\text{pixel}$ was selected to transform the results from the digital image to the physical dimension on the specimen surface.

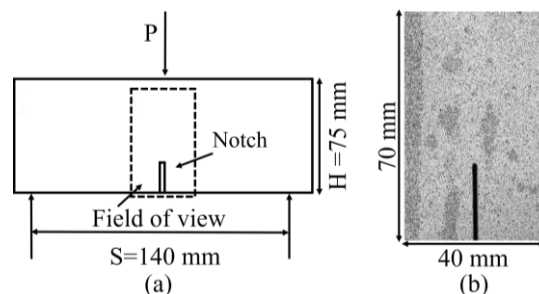


Figure 2. (a) Loading geometry and observation region on the specimen surface; (b) Digital image of the speckle pattern.

5. EXPERIMENTAL RESULTS

5.1 FPZ characterization using displacement field

DIC was used to characterize the evolution of the FPZ by analyzing full-field displacements over the specimen surface. Several studies, such as Lin et al. (2014), Ji et al. (2016), and Zhang et al. (2018) have shown the FPZ as the micro-cracking zone through the displacement continuity represented by the merging of DIC based displacement contours.

Figure 3 shows the distribution of the horizontal displacement field at (a) when 80% of the peak load was applied, (b) when the peak load was applied, and (c) when 95% of the peak load was applied during the post-peak stage of the test (i.e., 5% load drop from peak was reached). The measured displacements were calculated by DIC with the reference image taken at the beginning of the test. Therefore, the displacement fields presented in figure 3(a-c) represent the total horizontal displacement at the three different loading stages. A symmetric pattern for the displacement field was observed surrounding the notch tip ($x=0$) representing an elastic loading at 80% of the peak load (figure 3a). With the further application of the load and at the peak load stage, a fracture-like zone or displacement discontinuity was formed ahead of the notch tip, as shown by the merged position in the displacement contour (figure 3b). This displacement discontinuity is characterized as the FPZ (Lin et al., 2014; Ji et al., 2016; Lu et al., 2019) with its tip (figure 3b) representing a transitional zone between the FPZ and elastic deformation. During the post-peak stage of the test, the FPZ was found to extend (figure 3c) and will eventually form a traction free crack when displacement values in the merged region exceed critical opening. The process zone is considered to be fully developed at the time of the initiation of the traction free crack (macro-crack), resulting in an unstable crack propagation (Lin and Labuz, 2013; Ji et al., 2016).

In order to quantify the crack opening in the form of the displacement discontinuity, two vertical lines around the center notch with the distance of 4 mm from each other (figure 3c) were selected to represent the virtual surfaces of the crack plane. The horizontal (normal) displacements were calculated between these two lines (figure 3c) and not at the crack plane ($x=0$) because, in the context of DIC, an ideal (plane) fracture does not exist. A certain width that should be larger than the subset size can be selected to measure the crack displacement. The distance of 4 mm was selected, which is larger than the subset size of 1.5 mm.

Figure 3d shows the displacement between the two sides of the crack in the vertical direction starting from the notch tip (i.e., $y=26$ mm). The crack opening can be defined as the relative normal displacement between the

two sides of cracks (figure 3d). At 80% pre-peak load level, although displacement contours indicate the elastic deformation (figure 3a), the crack opening of 7.2 μm can be observed at the notch tip (figure 3d). Similarly, at the peak load, the merged position of the displacement contour, which occurred at $y=32$ mm (figure 3b), showed the crack opening of 8.5 μm (figure 3d). This indicated that the material under the elastic deformation had an associated opening displacement before the initiation of the process zone, and the tip of the process zone was not aligned with the merged position of the displacement contours. Similar observations were made by Lin et al. (2019a) based on mode I fracturing experiments on Berea sandstone. They characterized the FPZ using the cohesive zone model, which stated that the rock under uniaxial tension behaves elastically until the stress at the crack tip reaches the tensile strength with an associated threshold value of crack opening displacement. Therefore, it is critical to estimate the threshold value of elastic opening displacement (w_e) to exactly identify the stage of FPZ initiation.

Figure 3(a-c) clearly show that the merged position of the displacement contour moved upward with the increase in loading. Although the tip of the process zone is not aligned with the merged position of the displacement contour, the extent of FPZ is also increasing with the applied load. Figure 3e shows horizontal displacement profiles along the notch plane ($y = 26$ mm) at various loading stages. The displacement profiles clearly indicated an increase in the horizontal displacement gradient ($\partial U/\partial x$) with applied loading resulting from the evolution of the fracture process zone. Additionally, the crack opening displacement at notch tip, abbreviated as CTOD, increased with the applied load (figure 3(d-e)). When the CTOD exceeds the crack opening (w_c), a traction free crack initiates at the notch tip (Lin et al., 2014; Zhang et al., 2018). Most studies (Lin and Labuz, 2013; Ji et al., 2016; Zhang et al., 2018; Lu et al., 2019) assumed that the FPZ gets fully developed at the peak load and the traction-free crack (macro-crack) initiates at this stage that leads to unstable crack propagation. However, other studies such as Aggelis et al. (2013), Yu et al. (2018), Lin et al. (2019b) have found that the FPZ is partially developed at the peak load and thus traction free crack initiation occurs during the post-peak stage of the test.

In the current study, the CTOD was evaluated to characterize the initiation and evolution of the FPZ. Figure 4a shows the variations of the CTOD and the applied load with the beam deflection. Figure 4b shows the changes in the instantaneous slope of CTOD/deflection (mm/mm) with the applied beam deflection.

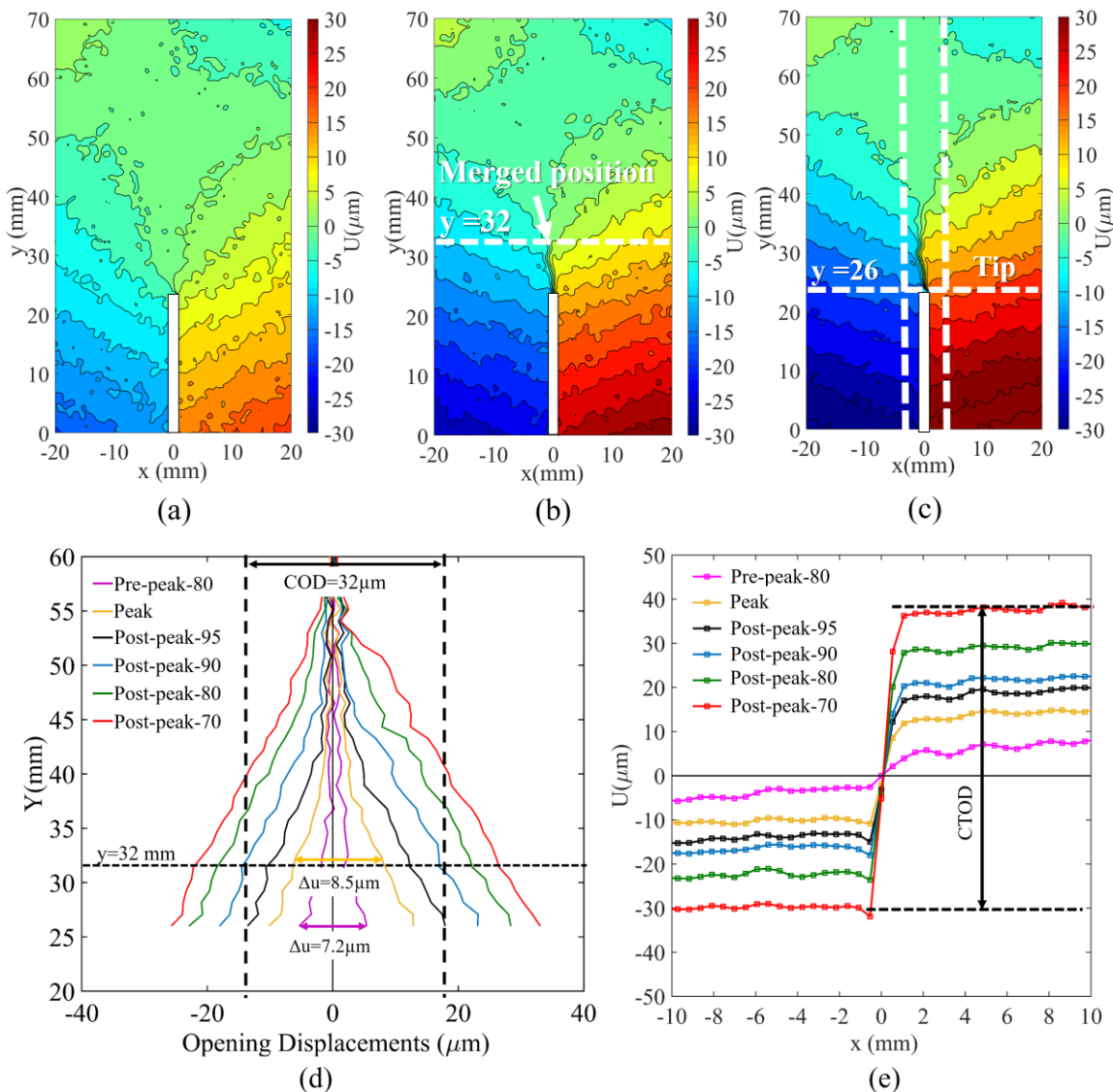


Figure 3. Horizontal displacement field. (a) Displacement contours at 80% of the peak load; (b) Displacement contours at the peak load; (c) Displacement contours for the post-peak stage when the load reached 95% of the peak value; (d) Crack opening displacement variations along the fracture from 80% pre-peak to 70% post-peak (e) Displacement profiles along the notch plane ($y = 26$ mm) at various loading stages.

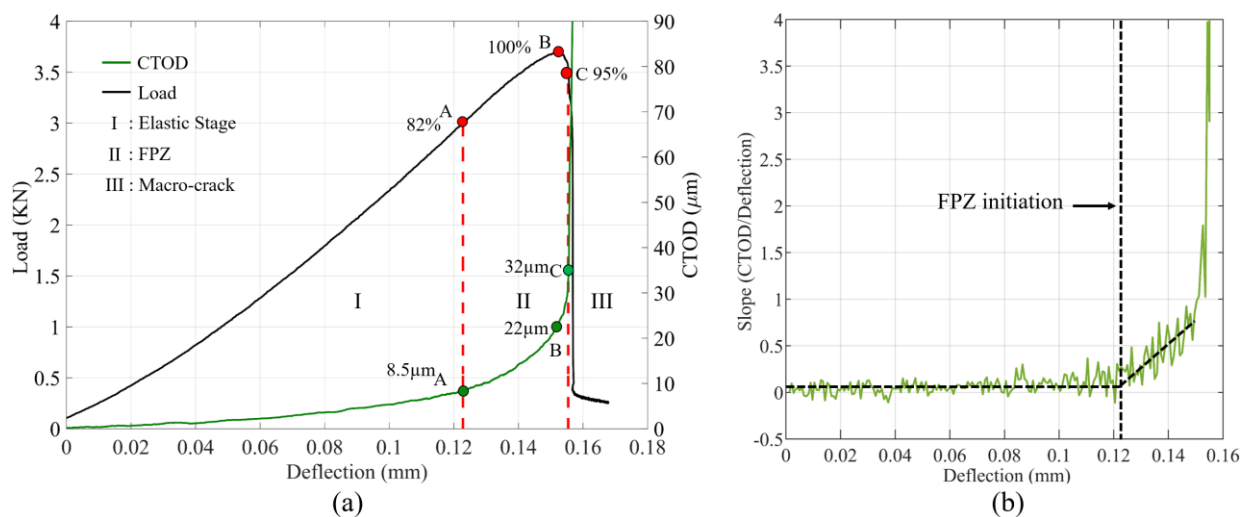


Figure 4. (a) Load and the crack tip opening displacement (CTOD) variations with the applied beam deflection showing three-stage from elastic deformation to macro-crack initiation; (b) FPZ initiation identified through the instantaneous slope of CTOD/deflection (mm/mm) with the beam deflection.

It is clear from figure 4(a-b) that the CTOD varied linearly with the beam deflection during the initial loading stage of the test representing the elastic deformation of rock near the notch tip. With further loading, the CTOD varied non-linearly with the first significant change in the rate of CTOD at point A in Figure 4a with the applied load level of 82% of the peak load. At this loading stage, the CTOD was around 8.5 μm represented by point 'A' on CTOD curve (figure 4a) and can be regarded as the elastic crack opening displacement ($w_e = 8.5 \mu\text{m}$). This increase in the rate of the CTOD can be associated with the FPZ initiation near the notch tip, resulting from the micro-cracks accumulation around the notch tip. Similar observations were made by Lu et al. (2019) based on mode I fracture experiments on sandstone. They showed that micro-cracking near the notch tip (FPZ initiation) resulted in a sharp increase in the rate of the crack opening displacement at the notch tip.

After the FPZ initiation at the notch tip, the CTOD increased at an accelerated rate with the increase in the load (Figure 4a), resulting in a continuous increase in the slope of the CTOD/deflection (mm/mm) with the beam deflection (Figure 4b). At point 'C' (see the CTOD curve in figure 4a), the CTOD jumped rapidly from 32 μm to 90 μm with a small change in the beam deflection (figure 4a). This rapid jump in the CTOD value can be attributed to the onset of the unstable crack propagation resulting from the initiation of traction-free crack at the notch tip. A similar criterion was used by Sharafisafa et al. (2019) and Aliabadian et al. (2019) to identify the macro-crack initiation stage. Therefore, CTOD of 32 μm at point 'C' can be considered as the critical opening displacement (w_c) for initiation of traction free crack. Interestingly, for the rock specimen tested, the macro-crack initiation occurred in the post-peak stage of the test and at the load level of 95% of the peak load, as shown by point 'C' in figure 4a. This observation is in agreement with other AE studies (Yu et al., 2018; Lin et al., 2019b) that suggests the initiation of traction-free crack during the post-peak stage of the test. Based on the CTOD variations with the applied beam deflection (figure 4a), cracking in the Barre granite can be divided in three phases: (I) the elastic deformation, (II) the FPZ initiation and its propagation, and (III) the traction-free crack that leads to unstable crack propagation. Table 1 summarizes the results of three center notch specimens tested in this study. As shown in Table 1, both the elastic and the critical crack opening displacement values were consistent and can be regarded as the material property for Barre granite under mode I loading. Additionally, the length of FPZ (fully developed) at the time of the initiation of the traction free crack was similar in all three tests. The observation is in agreement with the results of Lin and Labuz (2013) for Berea sandstone, which suggests that length fully developed of FPZ is constant for given rock.

Table 1: Experimental results for three center-notched tests.

Test #	CN-1	CN-2	CN-3	Average
Peak load (KN)	3.69	3.64	4.69	4
Elastic Opening (w_e) (μm)	8.5	4.5	5.8	6.3
FPZ initiation load (KN) (Pre-peak regime)	3.02	3.14	4.3	3.49
Critical opening (w_c) (μm)	32	30	36	33
Crack initiation load (KN) (Post-peak regime)	3.5	3.29	4.1	3.64
FPZ length (mm)	13.5	14.3	13.2	13.6

5.2 Cohesive zone model

The FPZ formed as a result of the micro-cracking zone around the crack tip can be idealized by the cohesive zone model for quasi-brittle materials (Karihaloo, 1995; Bazant and Planas, 1998; Lin et al., 2019). The cohesive zone model (Dugdale, 1960; Hillerborg et al., 1976) assumes the formation of an equivalent crack during the fracturing process, consisting of a real (traction-free) crack and a process zone (figure 5a). The FPZ also called the cohesive zone, is assumed as two crack surfaces that can still transfer the stresses across their faces as a function of the crack opening displacement (w).

The evolution of the fracture process in the cohesive zone model can be divided into four stages: (1) elastic stage, (2) FPZ initiation, (3) FPZ propagation (also called progressive failure) and (4) the traction-free crack (Xie et al., 2017; Zhang et al., 2019). Figure 5b shows the relation between the cohesive stress and the opening displacement (Ha et al., 2015; Zhang et al., 2018; Lin et al., 2019a). During the initial loading, stress at the crack tip increases until it reaches the tensile strength representing the elastic response of the material with the associated crack opening displacement, w_e . At this stage, the cohesive zone is formed ahead of the crack tip. With the further crack opening, the cohesive zone starts to soften, indicating the propagation of the FPZ. The softening of the cohesive zone can be characterized by the decrease in stress while increasing the crack opening displacement (figure 5b). When the critical opening displacement w_c is reached (figure 5b), the cohesive stress reaches zero, and a traction-free crack is formed. At this stage, the energy dissipated is called cohesive fracture energy (G_f) (Bazant and Planas, 1998; Xie et al., 2017), represented by the area under the entire cohesive stress and the opening displacement curve (figure 5b). Both elastic opening (w_e) and critical opening displacements (w_c) along with the size of the fracture process zone are considered material properties. In this study, parameters of the cohesive zone model such as elastic opening (w_e) and critical opening displacements (w_c) were estimated based on the evolution

of the crack tip opening displacement (CTOD) with the applied beam deflection (see section 5.1). The tensile strength of the material used in the cohesive zone model is typically estimated using Brazilian tests. The tensile strength of Barre granite (Table 2) was taken from the study by Iqbal and Mohanty (2007). The cohesive zone model was then validated using the numerical simulation of three-point bending tests of Barre granite.

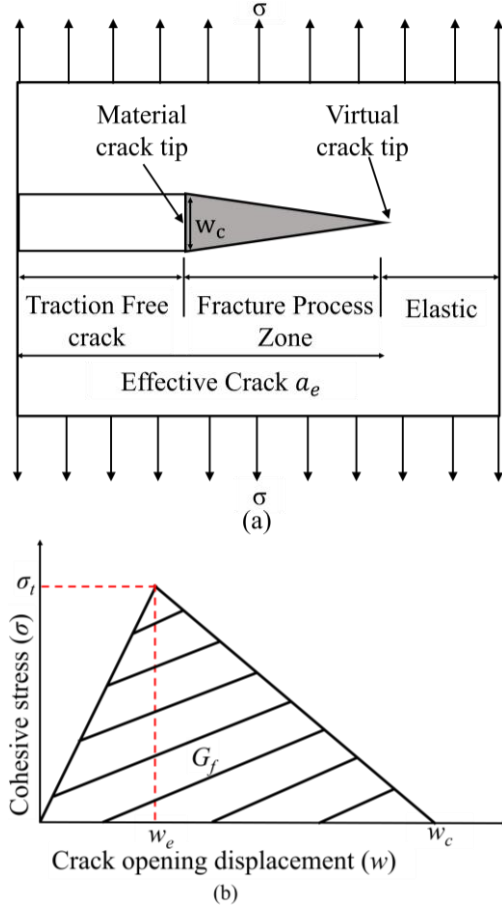


Figure 5. (a) Scheme of the effective crack along with cohesive zone; (b) Cohesive zone model for a unit length of FPZ in rocks (after Xie et al., 2017; Zhang et al., 2018).

6. NUMERICAL SIMULATION

6.1 Model description

The commercial general-purpose finite element package ABAQUS was used to simulate the crack propagation using the XFEM approach in the center notch Barre granite specimen. Figure 6 shows the 2D model of the three-point bend test on barre granite specimen. The modeled beam has the same dimensions as the experiment with the line crack representing the center notch of 26 mm. To simulate actual laboratory testing conditions, bottom rollers fixed in both x and y directions, and top rollers fixed in x-direction were used (figure 6). To model three-point bending, a displacement rate of 0.01 mm/step (1step=1sec) was applied at the top roller. The crack (notch) mouth opening displacement (CMOD) was recorded at the gage length of 6 mm in the numerical simulation. The model was discretized using a 4-node bilinear plane strain quadrilateral elements (figure 6). The

material properties of Barre granite used for simulating the crack propagation are listed in Table 2. The elastic parameters (E , ν) were calculated based on the compliance method by Hashida and Takahashi (1985). Various studies in rocks suggested different elastic modulus values under tension (E_t) and compression (E_c) due to inhomogeneity and existing micro-cracks (Li and Yin, 1998; Jianhong and Sun, 2008; Lin et al., 2019a). Using the Brazilian tests, these studies have found the ratio of E_t to E_c to range from 0.3 to 0.9 based on the rock type (Wang and Wu, 2004; You and Su, 2004; Jianhong and Sun, 2008). Additionally, studies such as Hashida and Takahashi (1985), Khoramishad et al. (2014) used the compliance method to determine the effective Young's modulus of granite under tension.

Table 2. Material properties of Barre granite

Parameter	Values
Young's modulus (E_t)	30 GPa
Poisson's ratio (ν)	0.16
Tensile strength (σ_t)	12.7 MPa
Elastic Opening (w_e)	6.3 μm
Critical opening (w_c)	33 μm

To simulate the crack initiation angle and propagation, the cohesive zone model, along with the maximum principal stress criterion, was used. The assumption is that the crack initiates in a direction perpendicular to the maximum principal stress. As mentioned earlier (section 5.2), the cohesive zone model incorporates the evolution of the fracture process from the notch tip in four stages: elastic stage, FPZ initiation, FPZ propagation, and traction-free crack. The elements will behave linearly elastic (figure 5b) until the principal stress exceeds the tensile strength of the material. This stage corresponds to the onset of fracture represented by damage initiation in Abaqus. This is followed by a reduction in cohesive traction of elements representing the fracture process zone. The softening of elements occurs with crack opening according to the curve shown in figure 5b. The elements undergo complete failure when separation exceeds critical crack opening (figure 5b) representing macro-crack initiation. Therefore, the fracture process zone is defined as the region of the progressive damage that lies between the position of the elastic separation and a critical crack opening (figure 5b) along the fracture surface.

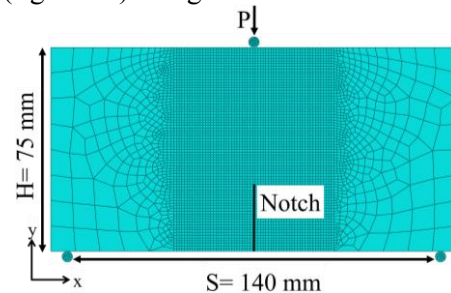


Figure 6. Model geometry for three-point bending test in Abaqus.

6.2 Analysis of Results and Discussion

Figure 7a shows the results of the experiments and simulations in terms of the applied vertical load versus the CMOD. This plot shows similar pre-peak responses among the three experiments and the numerical model. Among three experiments, scattering of peak load can be attributed to various factors such as heterogeneous material, notch length, grain size, etc. (Nasseri et al., 2010; Wang and Hu, 2017; Yu et al., 2018). Nasseri et al. (2010) showed that fracture toughness and crack location in heterogeneous rocks such as Barre granite is strongly influenced by microstructural anisotropy and grain size. As a result, granite rock specimens with smaller notches typically show large fluctuation in peak load (Wang and Hu, 2017).

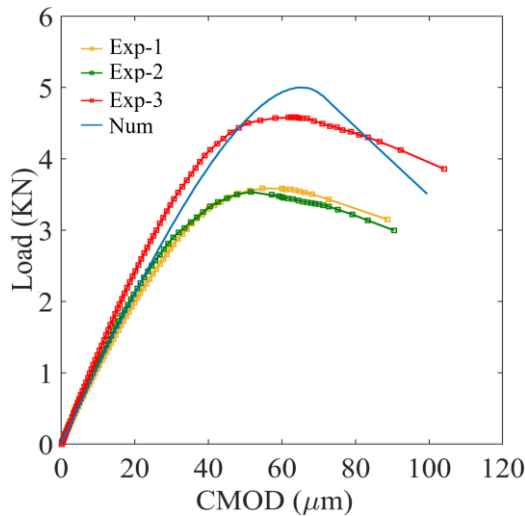


Figure 7a. Comparison between experimental and numerical results in terms of axial load vs crack mouth opening displacements (CMOD).

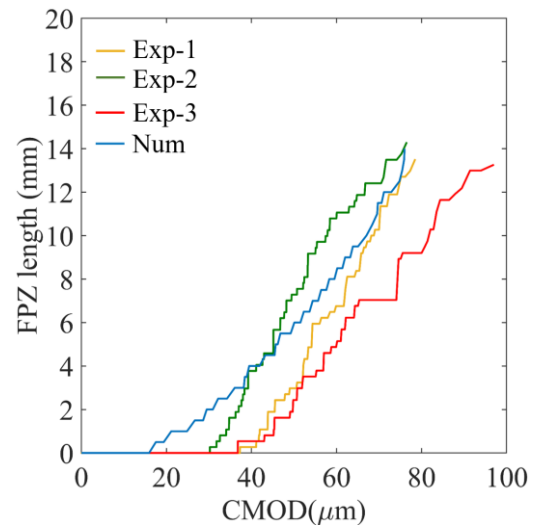


Figure 7b. Comparison between experimental and numerical results in terms of length of fracture process zone vs CMOD.

Further, for a given specimen size, as notch length increases, variation in peak load decreased as failure is controlled by the tensile strength of the material (Wang and Hu, 2017; Yu et al., 2018) as also called “boundary effect.” The difference in peak and post-peak response is between experiments, and the numerical model can be attributed to material heterogeneity and no calibration process in the current study. Various X-FEM based numerical model (Wang et al., 2013; Im et al., 2014) used a calibration process where parameters of cohesive zone model including cohesive fracture energy (G_f) and tensile strength (σ_t) are iteratively changed until the FE model results fitted the experimental results. In the current study, parameters of cohesive models were estimated (Table 2) from experiments and then directly used in the numerical model.

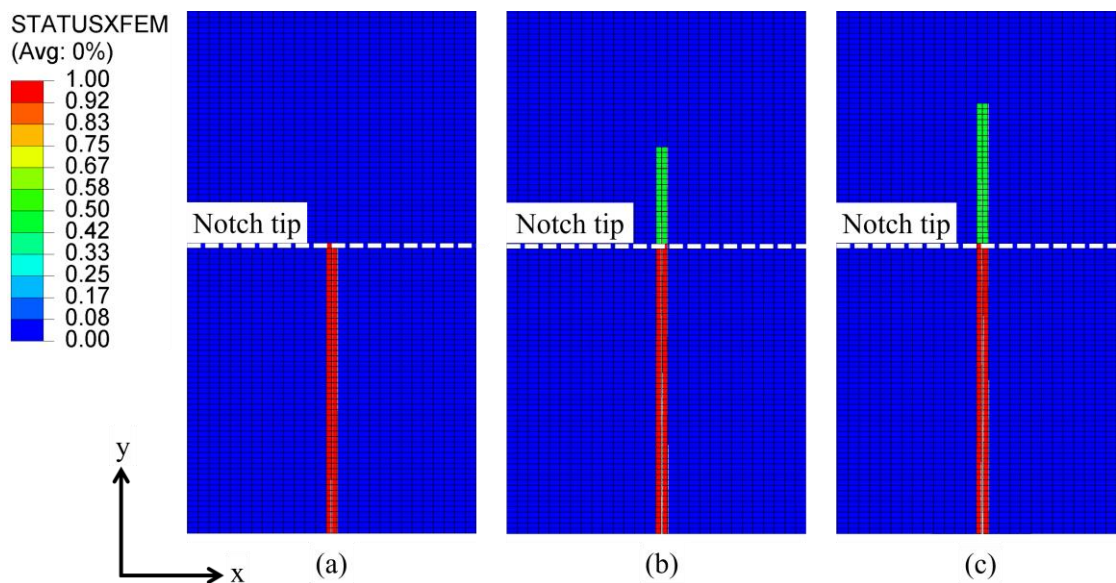


Figure 8. FPZ evolution in numerical model at (a) 35% of the peak value; (b) peak load; (c) post-peak stage when the load reached 93% of the peak value.

Additionally, fracture properties estimated from experiments are effected by material heterogeneities and natural fractures within the rock material. However, the three-point bending specimen used in numerical model is based on assumed of isotropic linear elastic material, which is a possible reason why the result determined using the peak load is greater than the experimental result.

Figure 7b shows the evolution of the FPZ until the macro-crack initiation stage for three experiments and the numerical simulation. In the numerical model, the fracture process zone is represented by elements undergoing progressive damage, denoted by STATUSXFEM parameter (figure 8a-c). The parameter indicates the status of the element with the values between 0 and 1. A value of 1 (red color in figure 8a-c) denotes “completely fractured or traction-free crack” while value 0 indicates an elastic state. The elements with the value between 0 and 1 indicate the elements under softening and thus represent the FPZ. Figure 8(a-c) clearly shows progression of FPZ at three different loading stages, namely (a) when 35% of the peak load, (b) when the peak load was applied, and (c) when 93% of the peak load was applied during the post-peak stage of the test (i.e., 7% load drop from peak was reached) is a stage just before macro-crack initiation. It is clear from figure 7b and table 3 that the FPZ initiation and propagation is scattered in three experiments which can attributed to material heterogeneity in Barre granite. For numerical simulation, average values of elastic opening (w_e) and critical opening displacements (w_c) were used (Table 1 and 3). As a results most of FPZ propagation obtained from numerical simulation lie within the three experiments data (figure 7b). However, significant difference was found in FPZ initiation stage between experiment and numerical model (figure 7b and table 3). The fracture process zone length at the initiation of traction free crack (also known as fully developed FPZ) was similar between experiments and numerical simulations (figure 7b and table 3). It can be concluded that numerical model showed similar FPZ evolution as occurred in three experiments.

Table 3. Comparison of experimental and numerical results

Test #	CN-1	CN-2	CN-3	Numerical model
Peak load (KN)	3.69	3.64	4.69	5
FPZ initiation load(KN) (Pre-peak regime)	3.02 (82%)	3.14 (86%)	4.3 (92%)	1.75 (35%)
Crack initiation load(KN) (Post-peak regime)	3.5 (95%)	3.29 (90%)	4.1 (87%)	4.65 (92%)
FPZ length (mm)	13.5	14.3	13.2	14

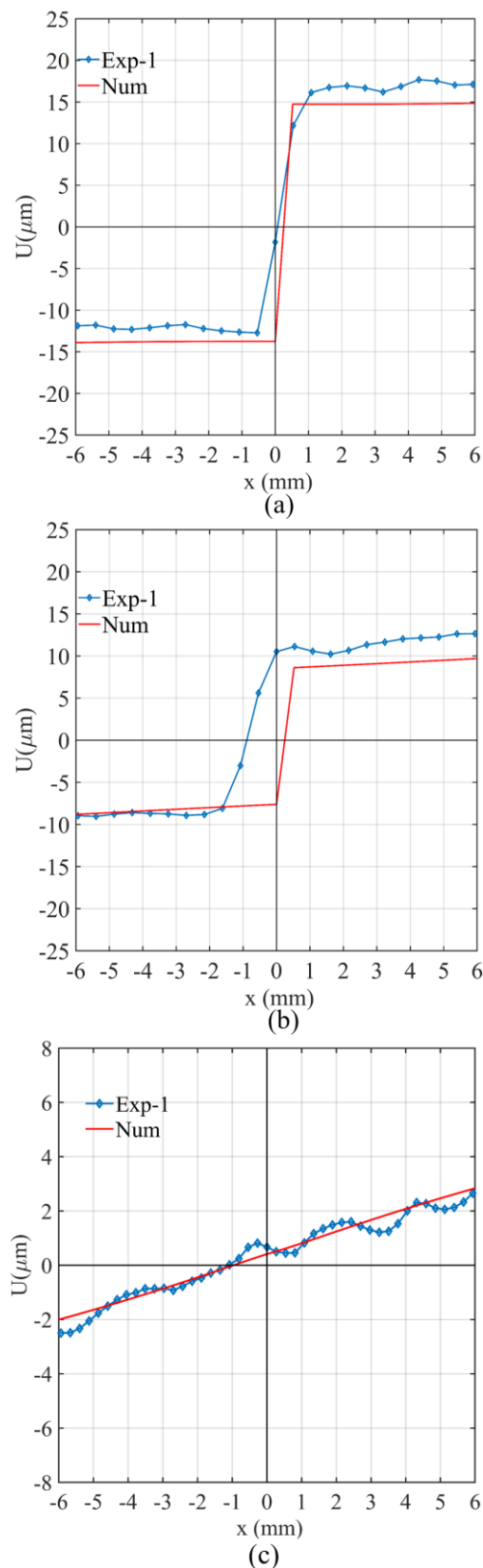


Figure 9. Horizontal displacement profile for the loading range of 95-92% of post-peak load in numerical model and physical experiments at (a) $y = 26$ mm, (b) $y = 32$ mm, (c) $y = 48$ mm.

The horizontal displacement profiles along horizontal lines were studied around the central part of the beam. Figure 9(a-c) shows the comparison between the experimental (DIC measurements) and the numerical data for horizontal lines located at different y values of 26 mm, 32 mm, and 48 mm. The displacement profiles were obtained at the load level corresponding to 95% of the peak load at the post-peak stage for the experiment and to 92% of the peak load at the post-peak stage for the numerical model. A relatively good match between the experimental and numerical data can be observed. In particular, at the notch tip ($y=26$ mm), a sharp jump or large opening displacement discontinuity was observed, representing the macro-crack initiation stage at that location. Similarly, at $y=32$ mm, a displacement discontinuity representing the fracture process zone was observed in both cases. At $y=48$ mm, a smooth transition in the horizontal displacement was observed, suggesting the elastic deformation at the location in both cases. Therefore, it can be concluded that the cohesive zone model estimated from three-point bending experiments on Barre granite can predict three stages of FPZ evolution with reasonably accuracy.

7. CONCLUSION

A series of three-point bending tests were performed on center notch Barre granite specimen. In order to characterize the evolution of the fracture process zone (FPZ), DIC imaging was used. Based on crack tip opening displacements (CTOD) variations, cracking in the Barre granite was divided into three phases: elastic deformation, FPZ initiation and its propagation, formation of traction-free crack that led to an unstable crack propagation. The cohesive zone model parameters were estimated by analyzing the full-field surface displacements obtained from 2D-DIC. The elastic opening (w_e) was estimated based on point of non-linearity in CTOD with applied beam deflection curve. While critical opening displacements (w_c) was estimated as point of rapid jump in CTOD (32 μm to 90 μm) with a small change in the beam deflection. In addition, the three-point bending test was simulated in ABAQUS using the XFEM approach with the cohesive zone model. The numerical results showed similar observations for the evolution of the fracture process zone in both experiments and numerical simulation. Additionally, the numerical simulation, similar to the experimental results, showed the traction-free crack initiation in the post-peak stage of the test. Therefore, it can be concluded that the experimentally validated cohesive zone model can accurately represent the FPZ around the notch tip in Barre granite

ACKNOWLEDGEMENTS

Funding for this research was provided by the National Science Foundation under award number 1644326. The authors are grateful for this support.

REFERENCES

1. Aggelis, D.G., Verbruggen, S., Tsangouri, E., Tysmans, T., Hemelrijck, D.V. (2013). Characterization of mechanical performance of concrete beams with external reinforcement by acoustic emission and digital image correlation, *Constr. Build. Mater*, 47, 1037–1045.
2. Aliabadian, Z., Zhao, G.F., Russell, A.R. (2019). Crack development in transversely isotropic sandstone discs subjected to Brazilian tests observed using digital image correlation. *Int J Rock Mech Min Sci*, 119, 211–221.
3. Bazant Z.P. and Planas, J. (1998) *Fracture and size effect in concrete and other quasi brittle materials*. Boca Raton, Florida: CRC Press.
4. Bazant, Z. P., Kim, J. K., and Pfeiffer, P.A. (1986). Nonlinear fracture properties from size effect tests. *Journal of Structural Engineering*, 112(2), 289–307.
5. Belytschko, T. and Black, T. (1999). Elastic crack growth in finite elements with minimal remeshing. *Int J Numer Methods Eng*, 45,601–620.
6. Corelated Solutions (2010b) *Vic-2D 2010 Reference Manual*. Columbia, SC, USA.
7. Dugdale, D.S. (1960). Yielding of steel sheets containing slits. *J Mech Phys Solids*, 8, 100–104.
8. Ghamgosar, M. and Erarslan, N. (2016). Experimental and numerical studies on development of fracture process zone (FPZ) in rocks under cyclic and static loadings, *Rock Mech. Rock Eng*, 49, 893–908.
9. Ghamgosar, M. and Erarslan, N. (2016). Experimental and numerical studies on development of fracture process zone (FPZ) in rocks under cyclic and static loadings, *Rock Mech. Rock Eng*, 49 893–908.
10. Gonçalves da Silva, B. and Einstein, H.H. (2013). Modeling of crack initiation, propagation and coalescence in rocks. *Int. J. Fract*, 182 (2), 167–186.
11. Ha, K. Baek, H. Park, K. (2015). Convergence of fracture process zone size in cohesive zone modeling. *Applied Mathematical Modelling*, 39 (19), 5828–5836.
12. Hashida, T. and Takahashi, H. (1985). *Journal of Testing and Evaluation* 13(1), 77–84.
13. Hedayat, A., Pyrak-Nolte, L., and Bobet, A. (2014c). Multi-modal monitoring of slip along frictional discontinuities. *Rock Mechanics and Rock Engineering*, 47(5), 1575–1587.
14. Hedayat, A., Pyrak-Nolte, L., and Bobet, A. (2014a). Precursors to shear failure of rock discontinuities. *Geophysical Research Letters*, 41, 5467–5475.
15. Hedayat, A., Pyrak-Nolte, L., and Bobet, A. (2014b). Detection and quantification of slip along non-uniform frictional discontinuities using digital image correlation. *Geotechnical Testing Journal*, 37 (5).
16. Hillerborg, A., Mode'er, M., and Petersson, P.E. (1976). Analysis of crack formation and crack growth in concrete by means of fracture mechanics and finite elements. *Cement and Concrete Research*, 6(6), 773–781.
17. Im S, Ban H, Kim YR. Characterization of mode-I and mode-II fracture properties of fine aggregate matrix using a semicircular specimen geometry. *Constr Build Mater* 2014;52(2):413–21.
18. Iqbal, M.J. and Mohanty, B. (2007). Experimental calibration of ISRM suggested fracture toughness measurement techniques in selected brittle rocks. *Rock Mech Rock Eng*, 40(5), 453.

19. Ji, W. W., Pan, Z.P., Lin, Q., Feng, T.X., Du, P.M. (2016). Do disk-type specimens generate a mode II fracture without confinement? *International Journal of Rock Mechanics and Mining Sciences*, 87, 48-54.
20. Jianhong, Y., Wu, F.Q., and Sun, J.Z. (2009). Estimation of the tensile elastic modulus using Brazilian disc by applying diametrically opposed concentrated loads. *International Journal of Rock Mechanics and Mining Sciences*, 46(3), 568-576.
21. Karihaloo, B.L. (1999). Size effect in shallow and deep notched quasi-brittle structures. *International Journal of Fracture*, 95(1-4), 379-390.
22. Khoei, A.R. (2014). *Extended finite element method: theory and applications*. John Wiley & Sons.
23. Khoramshad, H., Akbaridoost, J., and Ayatollahi, M. (2014). Size effects on parameters of cohesive zone model in mode I fracture of limestone. *International Journal of Damage Mechanics*, 23(4), 588-605.
24. Labuz, J.F., Shah, S.P., Dowding, C.H. (1987). The fracture process zone in granite: evidence and effect. *Int. J. Rock Mech. Min. Sci. Geomech. Abstr.* 24 (4), 235-246.
25. Li, B.Q. and Einstein, H.H. (2018). Correction to: Comparison of Visual and Acoustic Emission Observations in a Four Point Bending Experiment in Barre Granite. *Rock Mech Rock Eng* 51, 2979-2980.
26. Li, W. and Yin, J.G. (1998). A method for measuring both tensile and compressive elastic modulus of rock-like material. *Rock Soil Mech*, 19, 93-96.
27. Lin, Q. and Labuz, J. F. (2013). Fracture of sandstone characterized by digital image correlation. *Int. J. Rock Mech. Min. Sci.* 60, 235-245.
28. Lin, Q., Fakhimi, A., Haggerty, M., Labuz, F.J. (2009). Initiation of tensile and mixed-mode fracture in sandstone, *Int. J. Rock Mech. Min. Sci.* 46 489-497.
29. Lin, Q., Wan, B., Wang, S., Li, S., Fakhimi, A. (2019a). Visual detection of a cohesionless crack in rock under three-point bending. *Engineering Fracture Mechanics*, 211, 17-31.
30. Lin, Q., Wan, B., Wang, Y., Lu, V., Labuz, F.J. (2019b). Unifying acoustic emission and digital imaging observations of quasi-brittle fracture. *Theoretical and Applied Fracture Mechanics*, 103,
31. Lin, Q., Yuan, H., Biolzi, L., Labuz, J. F. (2014). Opening and mixed mode fracture processes in a quasi-brittle material via digital imaging. *Eng. Fract. Mech.* 131, 176-193.
32. Lu, Y., Li, W., Wang, L., Meng, X., Wang, B., Zhang, K., Zhang, X. (2019) In-situ microscale visualization experiments on micro-cracking and micro-deformation behavior around a pre-crack tip in a three-point bending sandstone. *International Journal of Rock Mechanics and Mining Sciences*, 114, 175-185.
33. Moës, N. and Belytschko, T. (2002). Extended finite element method for cohesive crack growth. *Eng Fract Mech*, 69(7), 813-33.
34. Morgan, S.P., Johnson, C.A., and Einstein, H.H. (2013). Cracking processes in Barre granite: fracture process zones and crack coalescence. *Int. J. Fract.* 180, 177-204.
35. Nasser, M.H., Grasselli, G., and Mohanty, B. (2010). Fracture toughness and fracture roughness in anisotropic granitic rocks. *Rock Mech Rock Eng*, 43(4), 403-415.
36. Pan, B., Asundi, A., Xie, H., Gao, J. (2009). Digital image correlation using iterative least squares and pointwise least squares for displacement field and strain field measurements. *Optics and Lasers in Engineering*, 47(7-8), 865-874.
37. Sharafisafa, M. and Nazem, M. (2014). Application of the distinct element method and the extended finite element method in modelling cracks and coalescence in brittle materials. *Comput Mater Sci* 91:102-121
38. Sharafisafa, M., Shen, L., and Xu, Q. (2018). Characterization of mechanical behaviour of 3D printed rock-like material with digital image correlation. *International Journal of Rock Mechanics and Mining Sciences*, 112, 122-138.
39. Shirole, D., Hedayat, A., and Walton, G. (2019a). Experimental relationship between ultrasonic attenuation and surface strains in prismatic rock specimens. *Journal of Geophysical Research: Solid Earth*, 124, 5770-5793.
40. Shirole, D., Hedayat, A., and Walton, G. (2019b). Influence of strain resolution on experimental correlation between ultrasonic amplitude and surface strains. *International Society of Rock Mechanics, Brazil*, 2019.
41. Shirole, D., Walton, G., and Hedayat, A. (2020b). Experimental investigation of multi-scale strain-field heterogeneity in rocks. *International Journal of Rock Mechanics and Mining Sciences*, 127, 104-212.
42. Sutton, M. A., Ortu, J., and Schreier, H. W. (2009). *Image correlation for shape, motion and deformation measurements*. New York: Springer.
43. Tarokh, A., Makhnenko, R., Fakhimi, A., Labuz, J.F. (2017). Scaling of the fracture process zone in rock, *Int. J. Fract.* 204 (2), 191-204.
44. Vasarhelyi, B. and Bobet, A. (2000). Modeling of crack initiation, propagation and coalescence in uniaxial compression. *Rock Mech Rock Eng* 33(2):119-39.
45. Wang H, Zhang C, Yang L, You Z. Study on the rubber-modified asphalt mixtures' cracking propagation using the extended finite element method. *Constr Build Mater* 2013;47(Complete):223-30.
46. Wong, L.N.Y. and Einstein, H.H. (2009b). Crack coalescence in molded gypsum and carrara marble: Part 1. macroscopic observations and interpretation. *Rock Mechanics and Rock Engineering*, 42, 475-511.
47. Wong, N.Y. (2008). *Crack Coalescence in Molded Gypsum and Carrara Marble*, Ph.D. Thesis. Massachusetts Institute of Technology.
48. Wu, Z, J. and Wong, L.N.Y. (2013). Modeling cracking behavior of rock mass containing inclusions using the enriched numerical manifold method. *Eng Geol*, 162, 1-13.
49. Yu, M., Wei, C., Niu, L., Li, S., Yu, Y. (2018). Calculation for tensile strength and fracture toughness of granite with three kinds of grain sizes using three-point-bending test. *PloS one*, 13(3).
50. Zhang, G., Xing, Y., Wang, L. (2018). Comprehensive sandstone fracturing characterization: Integration of fiber Bragg grating, digital imaging correlation and acoustic emission measurements. *Engineering Geology* 246:45-56.
51. Zhang, X.P. and Wong, L.N.Y. (2012). Cracking processes in rock-like material containing a single flaw under uniaxial compression: a numerical study based on parallel bonded-particle model approach. *Rock Mech Rock Eng* 45 711-37.